Original Article

The effect of tumor vascular remodeling and immune microenvironment activation induced by radiotherapy: quantitative evaluation with magnetic resonance/photoacoustic dual-modality imaging

Nan Xu[1#], Dan Wu[2#], Jingyan Gao[3#], Huabei Jiang[4], Qinqing Li[1], Shasha Bao[1], Yueyuan Luo[1], Qiuyue Zhou[2], Chengde Liao[5], Jun Yang[1]

[1]Department of Radiology, The Third Affiliated Hospital of Kunming Medical University, Yunnan Cancer Hospital/Center, Kunming, China; [2]School of Optoelectric Engineering, Chongqing University of Posts and Telecommunications, Chongqing, China; [3]Department of Radiation Oncology, The Third Affiliated Hospital of Kunming Medical University, Yunnan Cancer Hospital/Center, Kunming, China; [4]Department of Medical Engineering, University of South Florida, Tampa, USA; [5]Department of Radiology, Kunming Yan'an Hospital (Yan'an Hospital Affiliated to Kunming Medical University), Kunming, China

Contributions: (I) Conception and design: J Yang, N Xu; (II) Administrative support: J Yang, C Liao; (III) Provision of study materials or patients: D Wu, J Gao; (IV) Collection and assembly of data: S Bao, Y Luo, Q Li; (V) Data analysis and interpretation: H Jiang, Q Zhou; (VI) Manuscript writing: All authors; (VII) Final approval of manuscript: All authors.

[#]These authors contributed equally to this work.

Correspondence to: Prof. Jun Yang, PhD. Department of Radiology, The Third Affiliated Hospital of Kunming Medical University, Yunnan Cancer Hospital/Center, No. 519 Kunzhou Road, Xishan District, Kunming 650118, China. Email: imdyang@qq.com; Prof. Chengde Liao, PhD. Department of Radiology, Kunming Yan'an Hospital (Yan'an Hospital Affiliated to Kunming Medical University), 249 Renmin East Road, Panlong District, Kunming 650051, China. Email: chengdeliao@qq.com.

Background: Tumor radiotherapy combined with immunotherapy for solid tumors has been proposed, but tumor vascular structure abnormalities and immune microenvironment often affect the therapeutic effect of tumor, and multimodal imaging technology can provide more accurate and comprehensive information in tumor research. The purpose of this study was to evaluate the dynamic monitoring of tumor blood vessels and microenvironment induced by radiotherapy by magnetic resonance/photoacoustic (MR/PA) imaging, and to explore its application value in radiotherapy combined with immunotherapy.

Methods: The tumor-bearing mice were randomly allocated into six groups, which received different doses of radiation therapy (2 Gy ×14 or 8 Gy ×3) and anti-programmed death ligand-1 (PD-L1) antibody for two consecutive weeks. MR/PA imaging was used to noninvasively evaluate the response of tumor to different doses of radiotherapy, combined with histopathological techniques to observe the tumor vessels and microenvironment.

Results: The inhibitory effect of high-dose radiotherapy on tumors was significantly greater than that of low-dose radiotherapy, with the MR images revealing that the signal intensity decreased significantly ($P<0.05$). Compared with those in the other groups, the tumor vascular density decreased significantly ($P<0.01$), and the vascular maturity index increased significantly in the low-dose group ($P<0.05$). The PA images showed that the deoxyhemoglobin and total hemoglobin levels decreased and the SO_2 level increased after radiation treatment ($P<0.05$). In addition, the high-dose group had an increased number of tumor-infiltrating lymphocytes ($CD4^+$ T and $CD8^+$ T cells) ($P<0.01$, $P<0.05$) and natural killer cells ($P<0.001$) and increased PD-L1 expression in the tumors ($P<0.05$). The combination of radiotherapy and immunotherapy increased the survival rate of the mice ($P<0.05$), and a regimen of an 8 Gy dose of radiation combined with

immunotherapy inhibited tumor growth and increased the survival rate of the mice to a greater degree than the 2 Gy radiation dose with immunotherapy combination (P=0.002).

Conclusions: Differential fractionation radiotherapy doses exert biological effects on tumor vascular and the immune microenvironment, and MR/PA can be used to evaluate tumor vascular remodeling after radiotherapy, which has certain value for the clinical applications of radiotherapy combined with immunotherapy.

Keywords: Tumor microenvironment; tumor vasculature; radiotherapy; magnetic resonance imaging (MRI); photoacoustic imaging (PAI)

Submitted Feb 24, 2023. Accepted for publication Aug 14, 2023. Published online Sep 11, 2023.
doi: 10.21037/qims-23-229
View this article at: https://dx.doi.org/10.21037/qims-23-229

Introduction

Breast cancer has become one of the most common cancers in the world (1). It is highly heterogeneous and can be divided into different subtypes according to the status of the estrogen receptor (ER), progesterone receptor (PR) and human epidermal growth factor receptor 2 (HER2) (2). The successful application of immunotherapy strategies for treating some solid tumors provides new potential options for treating breast cancer. However, many clinical studies have found that low immune response rate and drug resistance are still problems with immunotherapy in the treatment of breast cancer (3-6). During tumor progression, the interactions between the tumor microenvironment and tumor cells mediate tumor immune tolerance, which affects the clinical effect of immunotherapy. The state of the tumor vasculature plays an important role in immunotherapy. For effective immunotherapy, sufficient T cells must sufficiently infiltrate tumor tissue; however, abnormal tumor vessels reduce immune cell infiltration through a variety of mechanisms, thereby limiting immunotherapy effectiveness. Moderate antitumor angiogenic therapy can correct the immature and chaotic blood vessels in the tumor, rendering tumor angiogenesis more dynamically balanced, and this improvement in vascular structure combined with immunotherapy drugs can lead to obvious therapeutic effects (7,8). However, the administration of antiangiogenic drugs can lead to many complications in the treatment of breast cancer and cannot effectively stimulate tumor immunogenicity, which limits their application in the comprehensive treatment of breast cancer (7).

Radiotherapy has been demonstrated to be effective for breast cancer (9). It can not only kill tumor cells but also directly promote immune-mediated tumor rejection by enhancing the total effect of tumor antigen processing and cross presentation, making tumor cells sensitive to immune recognition and attack, and increasing the immunosuppressive state of the tumor microenvironment, which promotes the recruitment, activation and action of T cells (10,11). In addition, angiogenesis is an important phenomenon in the progression of breast cancer and is mainly dominated by a variety of inflammatory factors. The level of angiogenic factors and subsequent angiogenesis may play a role in breast cancer metastasis and no recurrence or overall survival (12). Radiotherapy can prune but not completely destroy the vascular structure of the tumor (13), so that the distribution of blood vessels is more uniform, the interstitial pressure in the tumor tissue is reduced, and the oxygen content in the tumor tissue and the distribution of combined therapy drugs are maximized (14). Therefore, accurate evaluation of tumor vascular repair and microenvironmental changes is the key to the success of comprehensive treatment of breast cancer (15).

To date, imaging techniques such as dynamic contrast-enhanced magnetic resonance imaging (MRI), computed tomography (CT) perfusion imaging, sonography and nuclear medicine are often used to evaluate tumor vessels (16-18). Adequate detection of complex vascular changes is difficult with a single imaging method, although MRI and ultrasound are the measurements most reported in the clinical literature, and their reliability and stability are worthy of further observation. Photoacoustic imaging (PAI) is an emerging imaging technique that combines optics with ultrasound and can provide tissue structure and functional information. PAI has higher resolution than traditional ultrasonic imaging, namely, to the order of microns, which represents high-resolution tissue imaging (19). Second, PAI uses different tissues and components in the body to

reflect tissue structure and functional information by light absorption of different wavelengths (20). In addition, PAI can achieve noninvasive physiological and pathological imaging at the molecular level by combining molecular imaging probe technology and contrast-enhanced imaging technology (21). Compared with other functional imaging modes and techniques (positron emission tomography, scintimammography, color and power Doppler), PAI shows higher specific potential in the evaluation of benign and malignant breast masses, especially photoacoustic (PA) elastography, which can improve lesion detection. This may reduce the number of unnecessary biopsies for false-positive tests and benign masses, thereby reducing the burden on patients and the risk of radiological examination, and improving the cost-effectiveness of the test (22-24). Finally, through MRI to provide tumor structure information and PAI to provide perfusion information and tumor vascular information, hypoxia status and other functional information, we can accurately identify the changes in tumor blood vessels and the corresponding microenvironment (25,26). Hence, we conducted this study to evaluate whether magnetic resonance (MR)/PA can potentially be used to assess tumor vascular remodeling after radiotherapy and to observe changes in the immune-related tumor microenvironment at the molecular biological level with the aim of optimizing combination immunotherapy.

Methods

Cell line and animals

Mouse 4T1 breast cancer cells were provided by the Chinese Academy of Sciences Stem Cell Bank and cultured in RPMI-1640 (Gibco, Shanghai, China) containing 10% fetal bovine serum and penicillin–streptomycin. Female BALB/c mice (5–6 weeks old, weighing approximately 18–20 g) were purchased from the Department of Experimental Animals, Kunming Medical University. This study was approved by the Experimental Animal Ethics Committee of Kunming Medical University, in compliance with Yunnan Cancer Hospital Ethics Committee guidelines for the care and use of animals. Approximately 1×10^6 cells in 200 µL of phosphate-buffered saline (PBS) were inoculated subcutaneously in the right lower limb of the mice. Twelve days after implantation, these 4T1 mouse breast cancer models (V_{tumor} ≥200 mm^3) were used for treatment experiments. The tumor volume calculation formula was $V=0.5\times a\times b^2$, where a is the vertical long diameter measured by calipers and b is the vertical short diameter.

Tumor treatment

The tumor-bearing mice (TBM) were randomly allocated to six groups: the low-dose group, high-dose group, low-dose + anti-programmed death ligand-1 (PD-L1) group, high-dose + anti-PD-L1 group, anti-PD-L1 group and control group. Animals received 2 Gy ×14 (low-dose group) or 8 Gy ×3 (high-dose group) radiation for 2 consecutive weeks. The combination treatment groups were administered an anti-PD-L1 antibody [clone 10F.9G2, isotype rat IgG2b, Bio-Xcell (New Hampshire, USA)] by intraperitoneal injection (200 µg ×3, on days 12, 18, and 25), and the control group was injected with the same amount of normal saline and evaluated in a survival analysis. The TBM were exposed to X-ray radiation from an RS2000 Biological X-ray Biological Irradiator (Georgia, USA) with an accelerating voltage of 225 kV and a dose rate of 1.8 Gy/min. To prevent radiation exposure of normal tissue, the mice were immobilized in the irradiator, the area away from the tumor was covered by a lead screen, and the other parts of the body were covered with lead screens to minimize the radiation to normal tissues. Tumor volume and body weight were measured every 2 days.

MR/PA bimodal imaging and analysis

The mice from the radiotherapy group and the control group were scanned on days 12 and 26 with a 3.0 T MRI scanner (Ingenia, Philips Medical Systems, Amsterdam, The Netherlands). The mice were injected intraperitoneally with 200 µL of Mn-Au contrast agent (APN-AU-40, 50 mmol/L $MnCl_2$, and 7×10^{10} N/mL) 24 hours before imaging. During imaging, the mice in the prone position were anesthetized with 10% chloral hydrate administered intraperitoneally, and eight-channel phased array coils were used for scanning the animals. The tumor was placed in the center of the coil, and the Mn-Au contrast agent was placed in the opposite lower limb of the tumor for image signal intensity (SI) comparison. TSE-T1WI was performed with the following parameters: a repetition time (TR)/echo time (TE) of 510 ms/27 ms, an average signal number of 8, a slice thickness/slice spacing of 1.5 mm/0.15 mm, a slice number equal to 14, a flip angle of 90°, a scanning field of view (FOV) equal to 5 cm × 5 cm, a matrix of 200×198, and a total imaging time of 588 s. The image data were analyzed using software on multifunction workstations (Syngo.via,

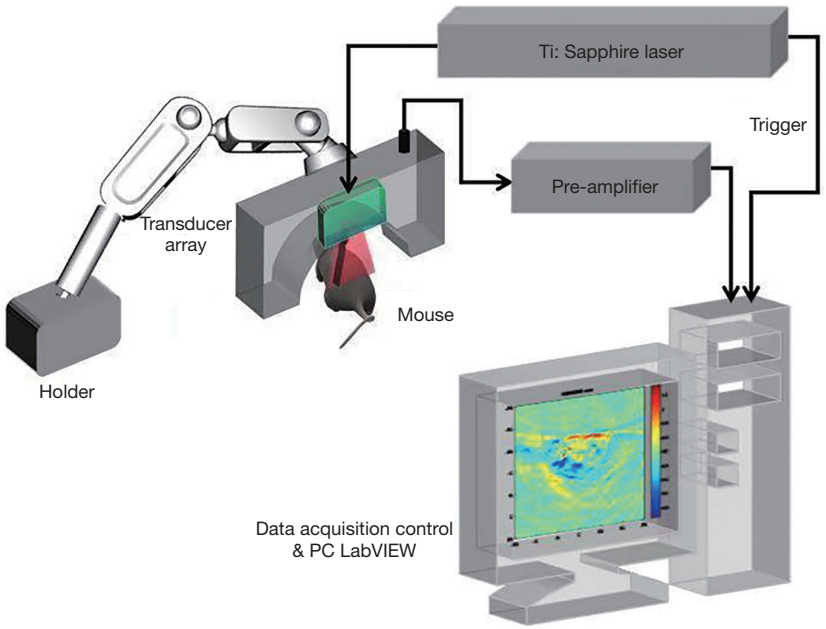

Figure 1 Schematic of our PAI system for *in vivo* imaging of TBM. PC, personal computer; PAI, photoacoustic imaging; TBM, tumor-bearing mice.

version VB10B, Siemens, Erlangen, Germany). The regions of interest (ROIs) were drawn manually on the tumor (including the periphery and center of the tumor) and the contrast agent on the image of one slice, and each ROI was approximately the same size (approximately 0.5 mm^2) and shape. The SI produced by the Mn-Au contrast medium was obtained. The mean signal of the contrast agent was standardized in each slice. The enhanced Mn^{2+} intensity in the peripheral and central tumor ROIs was calculated by the following formula: SI = SMn (Con) – SMn [$IP_{(per/c)}$]/SMn (air), in which SMn (IP_{per}), SMn (IP_c) and SMn (air) represented the SI of the peripheral and central Mn^{2+} of the tumor and the SI of the peripheral air, respectively. The resulting images were processed by background elimination and normalization. In the method of background elimination, MRI signals below the baseline were partly removed, and only the remaining signals were retained (incomplete background elimination). This method can improve the signal-to-noise ratio.

The raw PAI data in this study were obtained with an *in vivo* laboratory-built PAI image acquisition system (*Figure 1*). A laser (Surelite OPO, Continuum, USA) emitted pulses with a width of 6–7 ns and a wavelength of 690–960 nm at a repetition rate of 20 Hz to excite the target and thus produce PA signals. The energy of the pulsed light was controlled to extend 10 mJ/cm^2 below the surface of the animal's skin, which was well beneath the safety standard (20 mJ/cm^2). A 128 element half-ring ultrasonic array probe (with a center frequency of 5 MHz and a bandwidth of 75%, Japan Probe Co., Ltd., Japan) was used to receive the PA signal. The received PA signal was amplified with a preamplifier (gain of 54 dB and frequency range from 460 kHz to 9 MHz) made in house, and the signal was collected through data acquisition cards (NI 5105). Ten-time averaging of the signal minimized the laser energy instability, and thus, the image quality was improved, making the calculation of the tumor area more accurate. During the acquisition process, real-time imaging was realized with a LabVIEW panel. The PAI tumor images were reconstructed from the PA signals using a delay and sum reconstruction algorithm.

The PAI tumor images were reconstructed from PA signals using a delay and sum reconstruction algorithm. According to the algorithm, we identified changes in the cerebral deoxyhemoglobin (HbR), oxyhemoglobin (HbO_2) and oxygen saturation (SO_2), levels in tumor regions at two different wavelengths (760 and 840 nm). The absorption coefficient of HbR is higher than that of HbO_2 at 760 nm, while the absorption coefficient of HbO_2 is higher than that of HbR at 840 nm. The HbO_2, HbR and SO_2 changes were calculated pixel by pixel via Eq. [1] and Eq. [2], and the pixels were chosen according to the calculated total

hemoglobin (HbT) concentration: $C_{HbT} = C_{HbO_2} + C_{HbR}$, which was greater than 0.

$$SO_{2(x,y,z)} = \frac{C_{HbO_2(x,y,z)}}{C_{HbT(x,y,z)}} \quad [1]$$

$$\begin{bmatrix} \frac{C_{HbR}}{C_{HbO_2}} \end{bmatrix}_{(x,y,z)} = \left(\begin{bmatrix} \varepsilon_{HbR}(760) & \varepsilon_{HbO_2}(760) \\ \varepsilon_{HbR}(840) & \varepsilon_{HbO_2}(840) \end{bmatrix}^T \begin{bmatrix} \varepsilon_{HbR}(760) & \varepsilon_{HbO_2}(760) \\ \varepsilon_{HbR}(840) & \varepsilon_{HbO_2}(840) \end{bmatrix} \right)^{-1} \cdot \begin{bmatrix} \varepsilon_{HbR}(760) & \varepsilon_{HbO_2}(760) \\ \varepsilon_{HbR}(840) & \varepsilon_{HbO_2}(840) \end{bmatrix}^T \begin{bmatrix} \varnothing_{760}(x,y,z) \\ \varnothing_{840}(x,y,z) \end{bmatrix} \cdot k \quad [2]$$

Where C_{HbO2} and C_{HbR} are the HbO_2 and HbR concentrations; ε_{HbO2} and ε_{HbR} are the molar extinction coefficients (cm^{-1}/M); φ_{760} and φ_{840} are the PA signal amplitudes acquired at wavelengths of 760 and 840 nm; and κ is the proportionality coefficient, which is determined on the basis of the acoustic parameters and wavelength-dependent local light fluence. Notably, because of the unknown coefficient κ, the calculated C_{HbO2} and C_{HbR} values are relative, however, the SO_2 calculated from Eq. [1] is absolute. In each PAI parameter image, areas consisting of 20×20 pixels of the normal tissue surrounding the tumor, boundary of the tumor and internal tumor were selected as the three ROIs (ROI I, ROI II and ROI III). The mean pixel value of the ROIs was calculated. ROI I was used as the baseline for calculating the relative changes in ROI II and ROI III. In addition, to conveniently calculate the pixel value within the ROIs, regions outside the ROIs were assigned a pixel value of zero.

Tumor immunofluorescence

All mice were sacrificed by spinal dislocation. Tumor tissues were fixed with 4% paraformaldehyde and cut into 4-μm-thick sections after dehydration and embedment. In brief, specimens were incubated with anti-CD31 [1:500, Abcam (Shanghai, China), ab182981], anti-α-SMA [1:200, Servicebio (Wuhan, China), GB13044], anti-Ki-67 (1:200, Servicebio, GB111141), anti-HIF-1α [1:200, Cell Signaling Technology (Boston, USA), 36169T], and anti-PD-L1 (1:200, Servicebio, GB11339A) antibodies for staining. The slices were imaged with a Nikon Eclipse C1 fluorescence microscope and scanned and analyzed with a PANNORAMIC panoramic slice scanner (Shanghai, China) and Image-Pro Plus 6.0 analysis software (Version X; Media Cybernetics, Silver Springs, MD, USA). Tumor slices were divided into three equal areas, and the microvessel density (MVD) of each area was detected by CD31 staining of perivascular cells. The area was quantified on the basis of the total number of microvessels per unit area; similarly, the coverage of the perivascular cells stained for α-SMA in each area was calculated. The vascular maturity index (VMI) refers to the percentage of blood vessels stained with the anti-α-SMA antibody compared to the total number of blood vessels stained with CD31 (27-29). An apoptosis kit (Servicebio, G1501) was used to perform TUNEL assays and thus evaluate the number of apoptotic tumor cells. Tumor cell proliferation was quantitatively analyzed based on the percentage of the number of positive cells stained for Ki-67 in each tumor area compared to the total number of cells. The ratio of HIF-1α-positive cells to total cells per unit area was calculated to analyze tumor hypoxia, and the proportion of PD-L1-positive cells to total cells was analyzed.

Flow cytometry

To obtain a single-cell suspension, the tumor tissue was mechanically cut into small pieces and subjected to cell filtration. The number of single cells in suspension was counted, and the cells were stained with specific antibodies against CD4 [BioLegend (California, USA), clone GK1.5, 100408], CD8a (BioLegend, clone 53-6.7, 100707), CD16 (BioLegend, clone S17014E, 158007), CD3 (BioLegend, clone 17A2, 100273), CD163 (BioLegend, clone S15049I, 155308), FOXP3 (BioLegend, clone 150D, 320011), CD25 (BioLegend, clone PC61, 102015), CD68 [eBioscience (California, USA), clone FA-11, 25-0681-80], CD80 (eBioscience, clone 16-10A1, 11-0801-81), and CD56 [Santa Cruz (Texas, USA), clone 123C3, SC-7326]. The expression levels of CD4, CD8, tumor-associated macrophages (TAMs), regulatory T (Treg) cells, and natural killer (NK) cells were detected with an acoustic focus flow cytometer (Invitrogen Attune NxT, AFC2), and the data were analyzed using FlowJo software (Tree Star Inc., California, USA).

Western blot analysis

The apoptosis of tumor cells in the tumor microenvironment was detected by Western blotting. As previously described (30), the tumor tissue was mechanically lysed with RIPA cleavage buffer (Solarbio, Beijing, China). After 30 min of incubation on ice, the total protein was extracted from the cells, centrifuged for 15 min at 4 ℃ and 12,000 rpm, and quantified with a BCA protein assay kit (Biosharp, Hefei, Anhui, China). The protein in the supernatant was dissolved in 5× electrophoresis sample buffer at a ratio of 1:4, heated to a high temperature and stored at −20 ℃ until use. The isolated proteins were separated by polyacrylamide gel

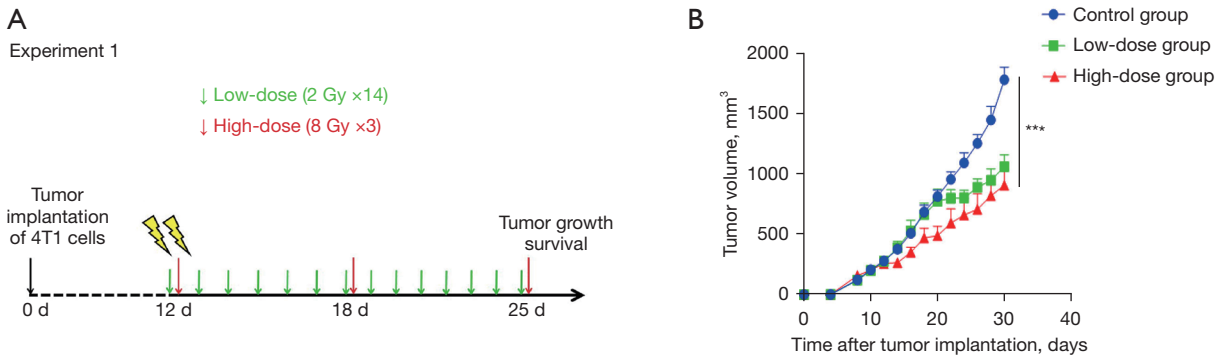

Figure 2 Tumor response to different doses of radiation therapy. (A) On the 12th day after tumor transplantation, TBM received different doses of radiotherapy (fractionated radiotherapy). (B) Tumor volume growth curve. ***, compared with the control group, P<0.001. TBM, tumor-bearing mice.

electrophoresis (Biosharp, Hefei, China), transferred to a polyvinylidene fluoride membrane (0.22 μm, Merck KGaA, Darmstadt, Germany), soaked in TBST (Solarbio) blocking solution containing 5% w/v skim milk (Biofroxx, Germany) for 2 hours, and then incubated for 0.5 hours with a primary antibody; horseradish peroxidase-bound secondary antibodies (1:10,000, Cell Signaling Technology, #7074) were added to the membrane and incubated for 1 hour at room temperature. Cleaved caspase-3 was visualized with an enhanced chemiluminescence enhancement kit (Biosharp), and the protein expression level was detected with ImageJ software (GE Healthcare Bio-Sciences, Uppsala, Sweden). The image was decolorized into an 8-bit black-and-white image, and its gray value represented the grayscale state of the image. The depth and area of the bands in the image comprehensively represented the amount of protein. Rabbit anti-cleaved caspase-3 antibody (1:1,000, Cell Signaling Technology, 9664) was used.

Statistical analysis

All data are expressed as the means±standard deviations (SD). Independent-samples *t*-tests, one-way ANOVA or nonparametric tests were performed to assess the differences between different groups. The correlation between MR/PA parameters and histological results was analyzed on the basis of Pearson correlation coefficients. SPSS 25.0 software (SPSS Company, Chicago, IL, USA) was used for the statistical analysis, and the survival data were analyzed with the Kaplan-Meier method; P<0.05 was considered statistically significant.

Results

Tumor volume

The changes in tumor volume were continuously observed after implantation of the breast cancer cells (*Figure 2A*). No significant difference in tumor volume was observed among the three groups before radiotherapy. On the 10th day, the tumor volume was 205.42±2.69 mm^3 in the control group, 199.08±2.18 mm^3 in the low-dose group and 203.33±1.79 mm^3 in the high-dose group. After fractionation radiotherapy, the percentage of tumor volume increased on the 26th day: it increased by 83.60% in the control group, by 77.59% in the low-dose group, and by 71.21% in the high-dose group. Compared with tumor progression in the control group, radiotherapy significantly inhibited tumor progression (P<0.001). The tumor growth in the high-dose group was lower than that in the low-dose group (P<0.001) (*Figure 2B*).

MR/PA imaging

MR images were obtained from each group of mice before and after radiotherapy. The images taken before radiotherapy showed no significant difference in signal intensity among the control group, low-dose group, and high-dose group (P>0.05). The radiotherapy group image showed a low enhancement area (*Figure 3A*), which significantly differed from that taken before radiotherapy. This finding suggested local necrosis inside the tumor. Although the images of the control group showed localized hypointense areas inside the tumor compared with those taken before radiotherapy, the difference in tumor signal change was not significant. Further analysis

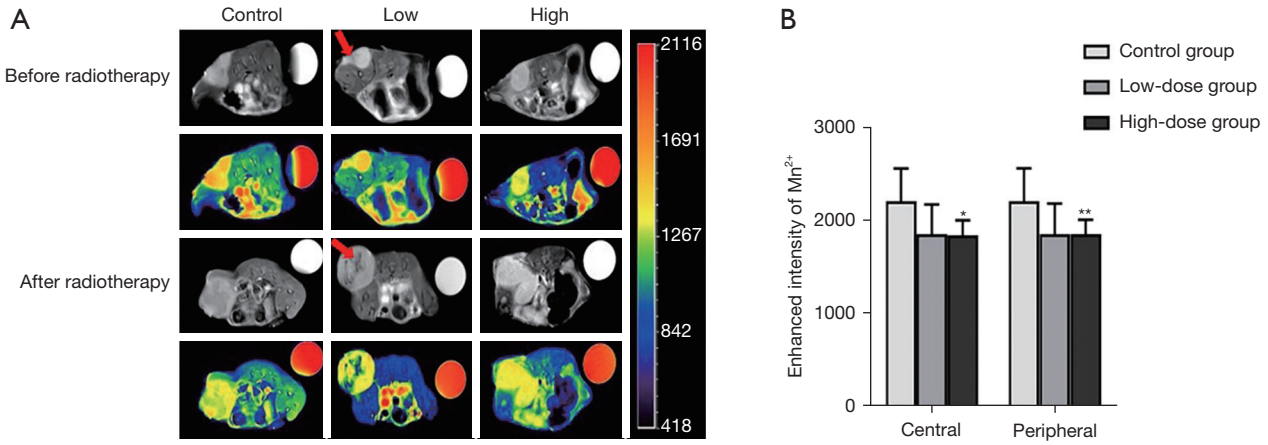

Figure 3 MR images before and after radiation in the therapy groups. (A) MR images of the control group, low-dose group, and high-dose groups before and after radiotherapy. The contralateral side of the tumor shows the Mn-Au contrast agent. The arrow indicates the necrotic area of the tumor. (B) Changes in signal intensity in the central and peripheral areas of the tumor after radiotherapy. The red arrow means the tumor area. *, compared with the control group, P<0.05; **, compared with the control group, P<0.01. MR, magnetic resonance.

showed that compared with that in the control group, the signal enhancement of the tumor center was decreased in the radiotherapy groups, and the SI decreased more significantly in the high-dose group (P<0.05) (*Figure 3B*). The SI in the peripheral region of the tumor was also decreased after radiotherapy (P<0.01) (*Figure 3B*).

In the PAI experiments, 5 representative images were continuously obtained for quantitative analysis, as shown in *Figure 4A*. The levels of HbT and HbR in the high-dose group and low-dose group were significantly lower than those in the control group (P<0.05) (*Figure 4B*). There was a significant difference in SO_2 between the high dose group and the control group (P<0.05). Further analysis showed that the levels of HbT (*Figure 4C*) and HbR (*Figure 4D*) in different regions of the tumor in the radiotherapy groups were different from those in the control group, but the levels of HbO_2 (*Figure 4E*) and SO_2 (*Figure 4F*) were not significantly different in different regions. In the high-dose and low-dose groups, the HbT levels in the central area of the tumor were lower than those in the peripheral region in the high-dose group (P<0.05), and the HbR levels in the central area of the tumor were lower than those in the peripheral region (P<0.05). There was no regional difference in HbT and HbR levels in the control group (P<0.05).

Immunofluorescence assay of the tumors

Compared with that in the control group, the number of Ki-67-positive proliferative cells decreased (P<0.01), and the number of TUNEL-positive apoptotic cells increased in both the low-dose and high-dose groups (*Figure 5*). Furthermore, in the high-dose group, the number of Ki-67-positive cells decreased most significantly (P<0.01), and the number of TUNEL-positive cells increased most significantly (P<0.05). In the high-dose group, Ki-67 was positively correlated with SI_{per} (r=0.879, P=0.021) and SI_c (r=0.938, P=0.006), but TUNEL staining was negatively correlated with SI_c (r=–0.867, P=0.025). In the low-dose group, Ki-67 was positively correlated with SI_{per} (r=0.826, P=0.043) and SI_c (r=0.907, P=0.012).

Tumor sections were stained with anti-CD31 and anti-α-SMA antibodies to detect tumor vessels (*Figure 5*). Compared with that in the control group, the number of blood vessels decreased; in the low-dose group to 48.93% (P<0.05), and in the high-dose group to 14.67%. In addition, compared with the control group, radiotherapy increased the VMI; in the low-dose group to 55.13% (P<0.05), and in the high-dose group to 29.60% (P>0.05).

Tumors were stained with anti-PD-L1 and anti-HIF-1α antibodies (*Figure 5*), and the effects of radiation on tumor immunity and hypoxia were evaluated. Compared with that in the control group, radiotherapy increased the expression of PD-L1 in the tumor by 25.69% in the low-dose group and 30.8% in the high-dose group, and the expression of PD-L1 in the high-dose group was significantly higher than that in the control group (P<0.05). Compared with the control group, radiotherapy slightly reduced the content of

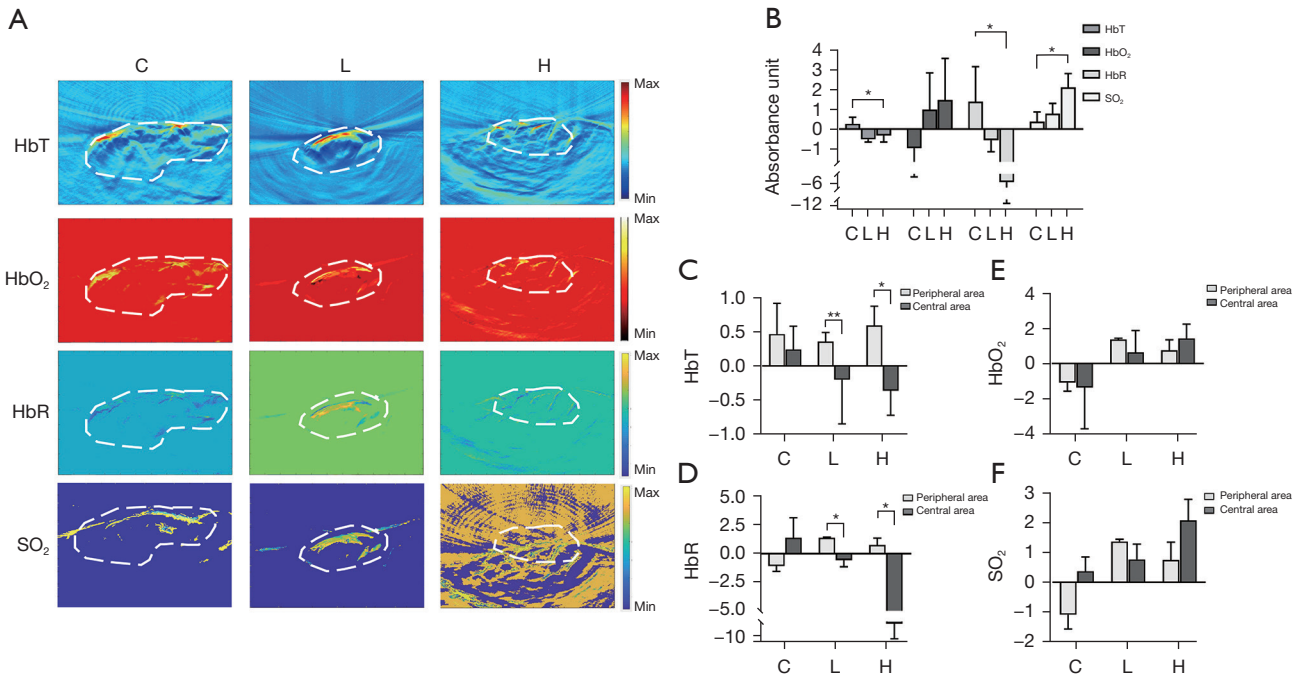

Figure 4 PA parameter image. (A) PA images of the control group, low-dose group, and high-dose group. (B) Signal intensity change of HbT, HbO_2, HbR, and SO_2 after radiotherapy, and (C-F) were the signal differences between the peripheral and central regions of the tumor. *, compared with the control group, P<0.05; **, compared with the control group, P<0.01. C, control; L, low; H, high; PA, photoacoustic; HbT, total hemoglobin; HbO_2, oxyhemoglobin; HbR, cerebral deoxyhemoglobin; SO_2, oxygen saturation.

HIF-1α in the tumor tissue (P>0.05).

Expression of cleaved caspase-3 in tumor tissue

Compared with the control group, the expression of cleaved caspase-3 in the high-dose group and low-dose group was significantly increased (P<0.01) (*Figure 6*).

Effect of radiotherapy on immune cells in tumors

To determine the changes in the number of tumor immune cells after radiotherapy, tumor-associated immune cells were analyzed by flow cytometry (*Figure 7*). Compared with the control group, the high-dose group showed an increase in $CD4^+$ cells of 73.96% (P=0.006), an increase in $CD8^+$ cells of 74.91% (P=0.015), and an increase in NK cells of 29.25% (P<0.001); the low-dose group showed an increase in $CD4^+$ cells of 67.46%, an increase in $CD8^+$ cells of 3.89%, and an increase in NK cells of 15.98% (*Figure 7A*,*7B*,*7E*). However, there was no significant difference in the levels of $CD4^+$, $CD8^+$, and NK cells between the low-dose group and the control group. In addition, no significant changes in TAMs (P=0.643) or Treg cells (P=0.932) were observed in the radiotherapy groups compared to the control group (*Figure 7C*,*7D*).

Therapeutic effects of the combination therapy on the tumors

To evaluate the efficacy of combination therapy, the mice were treated with anti-PD-L1 group (200 μg ×3 on days 12, 18, and 25), and high-dose + anti-PD-L1 group (8 Gy ×3, 200 μg ×3 on days 12, 18, and 25), and low-dose + anti-PD-L1 group (2 Gy ×14, 200 μg ×3 on days 12, 18, and 25) (*Figure 8A*). During treatment, the tumor growth in the three treatment groups was significantly lower than that in the control group (P<0.01). Compared with the anti-PD-L1 group, the low-dose + anti-PD-L1 group and high-dose + anti-PD-L1 group had significantly slower tumor progression (P<0.01) (*Figure 8B*). Compared with the control group regimen, the dose regimen of combined therapy showed a more significant inhibitory effect on tumor growth (P<0.01) and a tendency to increase the survival rate (P<0.01) (*Figure 8C*). Furthermore, compared

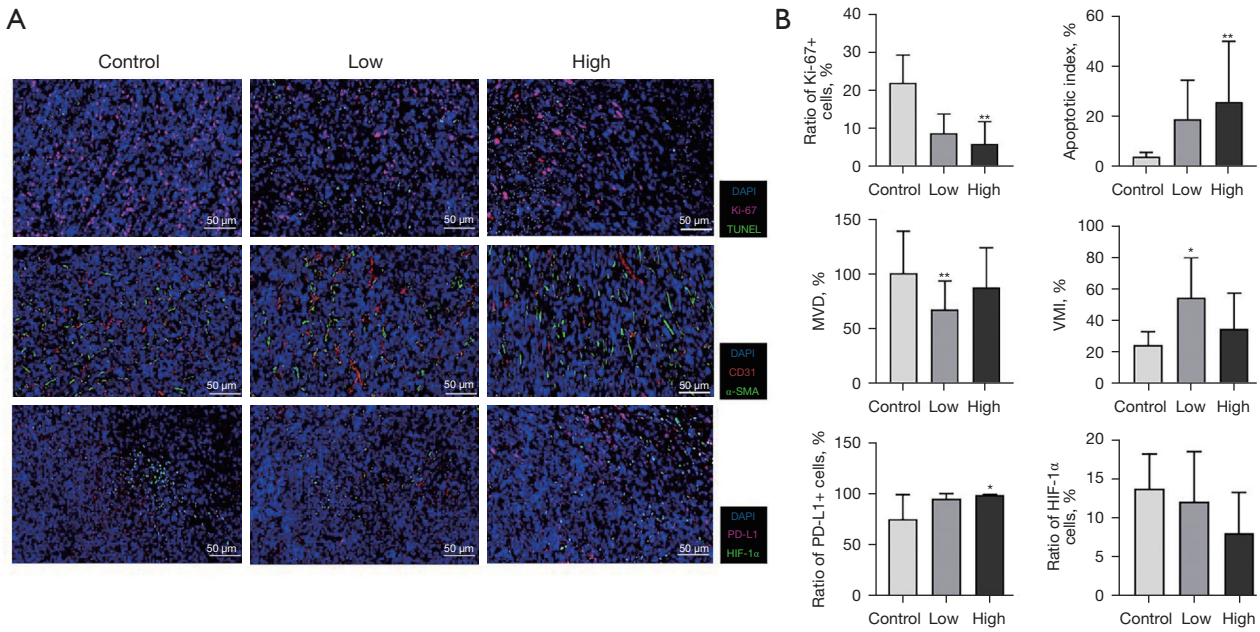

Figure 5 Effect of radiotherapy on tumor progression. (A) Double-marker immunofluorescence of Ki-67 (red) and TUNEL (green); the blue area represents the nucleus; double-marker immunofluorescence of CD31 (red) and α-SMA (green); double-marker immunofluorescence of PD-L1 (red) and HIF-1α (green); scale bar, 50 μm. (B) The percentages of Ki-67+ and TUNEL+ cells in the total number of tumor cells per unit area were measured, and cell proliferation and apoptosis were observed; quantitative evaluation of tumor MVD and VMI after radiotherapy; evaluation of tumor hypoxia and PD-L1 expression after radiotherapy. *, compared with the control group, P<0.05; **, compared with the control group, P<0.01. PD-L1, programmed cell death 1 ligand 1; MVD, microvessel density; VMI, vascular maturity index.

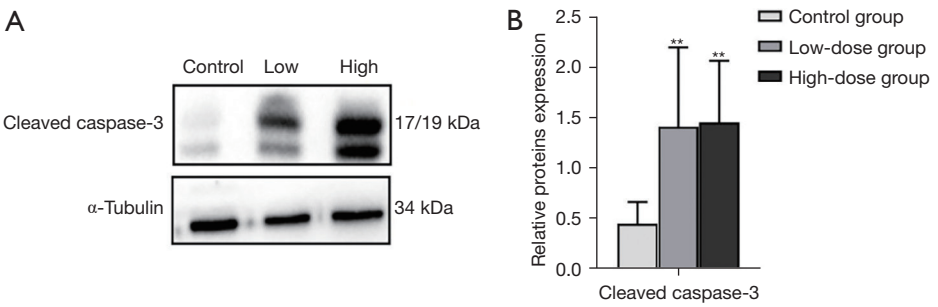

Figure 6 Effect of radiotherapy on tumor cell apoptosis. (A) Cleaved caspase-3 expression in tumors from different groups. (B) Histogram after quantitative analysis performed with ImageJ software. **, compared with the control group, P<0.01.

with the anti-PD-L1 group, the survival of the low-dose + anti-PD-L1 group was significantly increased (P=0.035), and this increase in the survival rate was the most obvious in the high-dose + anti-PD-L1 group (P=0.002).

Discussion

In this study, radiotherapy-induced tumor vascular remodeling by changing the vascular density and oxygenation level and increased the infiltration of immune cells and the expression level of PD-L1 in tumors, thus promoting the inhibition of tumor immune environment activation. Compared with histopathological biopsy, noninvasive quantitative imaging provides anatomical and vascular information on the tumor response to radiotherapy. To our knowledge, this is the first study to use MR/PA bimodal imaging to observe the response of tumor vessels and the microenvironment to different radiotherapy

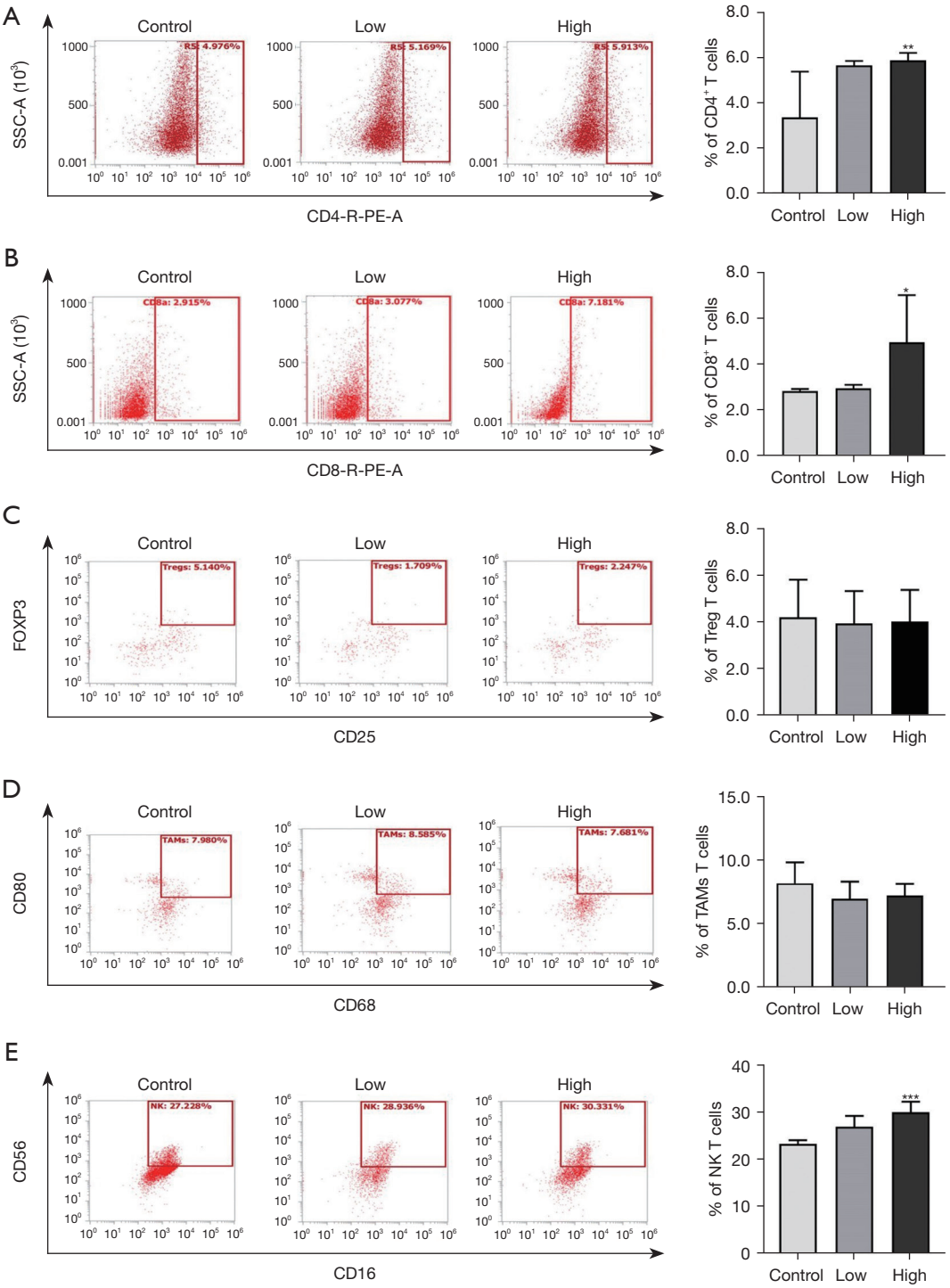

Figure 7 Flow cytometry of immune cells in tumors after radiotherapy. Flow cytometry quantitative data analysis revealed the number of tumor CD4⁺ T cells (A), CD8⁺ T cells (B), Treg T cells (C), TAM T cells (D) and NK T cells (E) after radiotherapy. Compared with the control group, *, P<0.05; **, P<0.01; ***, P<0.001. TAMs, tumor-associated macrophages; NK, natural killer.

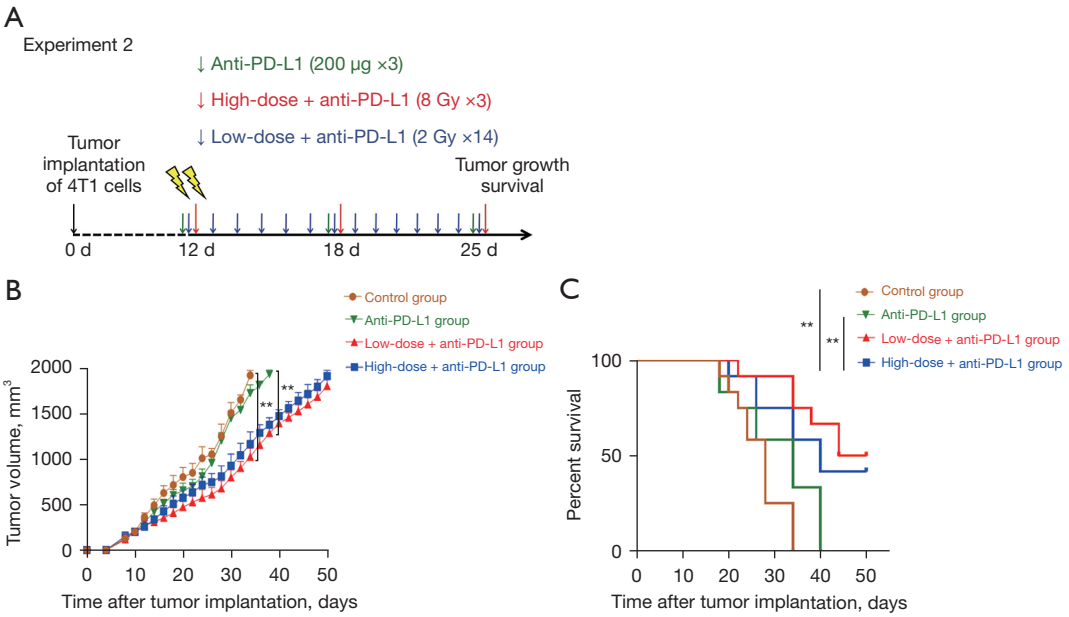

Figure 8 Tumor response to different doses of radiation therapy combined with immunotherapy. (A) On the 12th day after tumor transplantation, TBM received different doses of radiotherapy and immunotherapy. (B) Tumor volume growth curve. (C) Survival of mice with different tumor treatment regimens. **, compared with the control group, P<0.01. PD-L1, programmed death ligand-1; TBM, tumor-bearing mice.

regimens in TBM.

Tumor growth is affected in many ways during radiotherapy, and the differences in the radiotherapy fractionation scheme are important factors in controlling tumor progression and metastasis. In this study, we found that tumor growth was continuously inhibited by radiotherapy, and the effect of high-dose fractionated radiotherapy was more obvious than that of low-dose fractionated radiotherapy. Of course, this effect may have been related to our radiotherapy program. The inhibitory effect of low-dose fractionated radiotherapy on tumor cell growth was short-lived and weak, while interval high-dose fractionated radiotherapy can cause a wide range of DNA double-strand breaks, destroy the ability of cellular self-repair, and thus accelerate tumor cell apoptosis. Therefore, we should not only ensure the inhibitory effect of high-dose radiotherapy on tumor growth but also consider the interval of treatment. Ki-67 expression, the best marker of cell proliferation, and apoptosis marker expression were assessed to compare the effects of dose differences on tumor growth. The apoptosis index significantly increased, indicating that high-dose irradiation caused tumor cell death and effectively prevented tumor cell proliferation. In addition to analyzing the growth status of tumors, we also used manganese-enhanced MRI to monitor the changes in apoptosis of tumor cells after radiotherapy. Manganese ions are actively transported to biologically active cells through calcium channels, so T1-weighted positive signals of MRI were used to reflect the survival status of cells, especially to observe the response of tumor cells to different doses of radiotherapy (31,32). Compared with that of low-dose radiotherapy, the killing effect of high-dose fractionated radiotherapy on tumor cells was more direct and persistent. After high-dose radiotherapy, the degree of signal enhancement in the tumor center was decreased significantly, and the peripheral area of the tumor was more sensitive to high-dose radiotherapy and showed little enhancement, suggesting that the tumor cells in the peripheral region underwent apoptosis at a significant rate. More importantly, through MRI, we found that the radiosensitivity in different regions of the tumor differed. This finding may have been a result of phenotypically and genetically diverse tumor cell populations, and the proliferation rate and therapeutic sensitivity of these cells may differ (33). In addition, when tumor cells recruit stromal cell groups, such as immune cells and endothelial cells, the tumor microenvironment is remodeled, resulting in spatial variation within the tumor (34). The resulting spatial distribution of tumor and stromal cells leads to the progression of different

physiological subregions in tumors and differences in the resistance of tumor areas to treatment. The SI in the MRI of the tumors was positively correlated with Ki-67 staining and negatively correlated with TUNEL staining, which indicated that MRI can potentially be used to monitor tumor growth inhibition induced by radiotherapy and to help evaluate the sensitivity of tumor cells to the radiation dose.

Many aspects of vascular biology are affected by radiation and vary according to the dose/grade, time, and model studied (35). Radiotherapy may preferentially prune poorly covered/functional vessels to redistribute blood vessels, but this vascular change may not systematically translate into long-term effects on the tumor (36,37). Compared with a single dose of high-intensity irradiation, our 2 Gy ×14 and 8 Gy ×3 doses did not cause severe irreversible damage to tumor vessels. After 2 Gy ×14 treatment, the VMI was increased because of the effective stimulation, which may have been related to the retention and improvement of vascular system formation on the first few days after radiotherapy (38). After 8 Gy ×3 exposure, the MVD did not decrease significantly, possibly because of the death of vascular endothelial cells to varying degrees, which would have been quickly attenuated by the formation of new blood vessels, emphasizing the contribution of the fractionated radiotherapy scheme to tumor vessel remodeling.

The multiple effects of radiation on the tumor microenvironment include the regulation of the hypoxic state (39). HIF-1α is the main regulator of hypoxic transcription, which can be stably expressed in the hypoxic tumor state and promote the continuous differentiation of tumor cells and angiogenesis (40). The expression level of HIF-1α can indirectly reflect changes in tumor hypoxia (41). There was no significant change in the expression of HIF-1α after 2 and 8 Gy exposure. This outcome may have been due to the reoxygenation of tumor parenchyma cells that survived radiotherapy, an outcome that largely depends on the radiation scheme (42). A complex dose–response relationship between radiation-injured tumor vessels, tumor cell reoxygenation and reaggregation is suggested. During PAI monitoring of tumors after radiotherapy, we found that the contents of HbT and HbR in tumor vessels decreased and SO_2 increased in the high-dose group, suggesting that the morphology and oxygenation level of tumor vessels was affected to varying degrees, which may depend on the size of tumor vessels (43). The difference in the response of tumor vessels to different doses of radiation reflects the spatial heterogeneity of the tumor, especially the changes in blood vessel density and oxygenation level and the redistribution of blood flow. Syed and others called the physiological tumor habitat, and differences in imaging and histological findings are evident among different vascular and cellular tumor habitats (44). In general, the PAI parameters confirmed vascular degenerative changes after radiotherapy and were able to detect subtle changes in tumor oxygenation levels with high sensitivity, suggesting that the degree of vascular degeneration is related to radiotherapy dose, radiation-dose fractionation, regional tumor heterogeneity and other factors.

As an immunomodulator, radiation can directly stimulate immune cells to produce cytokines and chemokines that affect the local immune response, and this immune response varies on the basis of the radiotherapy program and tumor model (45-47). The activation status of T and NK cells is suggestive of antitumor immunity; immune cells can kill target cells via various mechanisms following activation. Radiation can enhance the cytokine secretion and cytotoxic activity of NK cells (48). Compared with the 2 Gy ×14 treatment, the 8 Gy ×3 treatment better promoted NK-cell recruitment to the tumor microenvironment, which may have been due to an increase in the radiation dose that was conducive to the release of tumor exosomes, promoting NK-cell polarization (49,50). According to our results, compared to the low dose, 8 Gy ×3 can better promote the aggregation of $CD4^+$ T cells and $CD8^+$ T cells in the tumor. The $CD4^+$ T-cell population contains effector T cells and Treg cells, which play roles in immune stimulation and immunosuppression, respectively (51), and the Treg cell subpopulation was not significantly changed after irradiation, but overall, high-dose radiotherapy seemed to disrupt the balance of the $CD4^+$ T-cell populations. In addition, the mechanism by which high-dose radiation affects $CD8^+$ T cells involves the promoted infiltration of immune cells into tumors through vascular endothelial cells or through the local production of chemical inducers (52). TAMs undergo two types of polarization, and TAMs undergoing M2-like polarization show inhibited production of immune cytokines (53). However, different doses of radiotherapy can lead to conflicting effects on TAM polarization; no significant change in TAMs was observed in this study, and therefore, further study and evaluation of the relative contribution of radiotherapy to TAM polarization types are needed.

PD-L1 has been proven to be a key immune checkpoint molecule expressed on the surface of immune cells and highly expressed on the surface of cancer cells. PD-L1

enables tumor cells to escape the host immune response by inducing T-cell depletion and inhibiting effector T-cell function (54). We found that 8 Gy ×3 radiotherapy triggered more PD-L1 expression than 2 Gy ×14, which suggested that high-dose fraction radiotherapy may induce a greater local inflammatory response in tumor tissue and enhance tumor-specific T-cell infiltration in the tumor microenvironment (55). Notably, the negative regulation of immune cells by PD-L1/programmed death 1 (PD-1) may be an important host-mediated mechanism of tumor-acquired radiation resistance, and the expression of PD-L1 induced by radiotherapy indicates an opportunity for the subsequent application of PD-L1/PD-1 axis inhibitors. However, due to the suppressed state of the tumor immune microenvironment, PD-L1 antibody drugs alone cannot exert the best effect in tumors, and immunotherapy alone is rarely used in clinical tumor treatment strategies. Combination therapy enhances the antitumor immunity of the host and improves the curative effect of the respective treatments (55,56). In our study, radiotherapy combined with an anti-PD-L1 antibody regimen effectively controlled tumor progression. In terms of survival rate, the radiotherapy dose regimen of 8 Gy ×3 was slightly better than that of 2 Gy ×14 for immunoregulation. Some studies have suggested that the dose-grading regimen of immune checkpoint drugs with 8 Gy ×3 radiation exposure should be the standard grading scheme for an immunotherapy combination (57-59). However, a consensus on the best radiation doses and fractionation plan has not been reached. Our study only compared immunotherapy alone with combination therapy, and preliminarily explored the effects of differences in radiation doses and fractionation plans in a combination treatment of breast cancer. The best plan for combined radiotherapy and immunotherapy needs to be assessed considering many variables, such as the effect of tumor subtype, immune response of the tumor and immunotherapy type, and the specific mechanism of action of radiotherapy in combination therapy. This will be the focus of future research.

Conclusions

In short, differential fractionated radiotherapy doses exert biological effects on tumor vascular remodeling and the immune microenvironment. MR/PA bimodal imaging can be used as an imaging marker to evaluate tumor vessels after radiotherapy and better guide the combined immunotherapy strategy of tumors.

Acknowledgments

Funding: This study was supported by the National Natural Science Foundation of China (No. 82060313), and the Outstanding Youth Science Foundation of Yunnan Basic Research Project (No. 202201AW070002).

Footnote

Conflicts of Interest: All authors have completed the ICMJE uniform disclosure form (available at https://qims.amegroups.com/article/view/10.21037/qims-23-229/coif). The authors have no conflicts of interest to declare.

Ethical Statement: The authors are accountable for all aspects of the work in ensuring that questions related to the accuracy or integrity of any part of the work are appropriately investigated and resolved. This study was approved by the Experimental Animal Ethics Committee of Kunming Medical University, in compliance with Yunnan Cancer Hospital Ethics Committee guidelines for the care and use of animals.

References

1. Sung H, Ferlay J, Siegel RL, Laversanne M, Soerjomataram I, Jemal A, Bray F. Global Cancer Statistics 2020: GLOBOCAN Estimates of Incidence and Mortality Worldwide for 36 Cancers in 185 Countries. CA Cancer J Clin 2021;71:209-49.
2. Loibl S, Poortmans P, Morrow M, Denkert C, Curigliano G. Breast cancer. Lancet 2021;397:1750-69.
3. Gerard CL, Delyon J, Wicky A, Homicsko K, Cuendet MA, Michielin O. Turning tumors from cold to inflamed to improve immunotherapy response. Cancer Treat Rev 2021;101:102227.
4. Bianchini G, Balko JM, Mayer IA, Sanders ME, Gianni L. Triple-negative breast cancer: challenges and opportunities

of a heterogeneous disease. Nat Rev Clin Oncol 2016;13:674-90.
5. Emens LA. Breast Cancer Immunotherapy: Facts and Hopes. Clin Cancer Res 2018;24:511-20.
6. Li Y, Zhang H, Merkher Y, Chen L, Liu N, Leonov S, Chen Y. Recent advances in therapeutic strategies for triple-negative breast cancer. J Hematol Oncol 2022;15:121.
7. Jain RK. Antiangiogenesis strategies revisited: from starving tumors to alleviating hypoxia. Cancer Cell 2014;26:605-22.
8. Mpekris F, Baish JW, Stylianopoulos T, Jain RK. Role of vascular normalization in benefit from metronomic chemotherapy. Proc Natl Acad Sci U S A 2017;114:1994-9.
9. Piruzan E, Vosoughi N, Mahdavi SR, Khalafi L, Mahani H. Target motion management in breast cancer radiation therapy. Radiol Oncol 2021;55:393-408.
10. Citrin DE. Recent Developments in Radiotherapy. N Engl J Med 2017;377:1065-75.
11. Potiron V, Clément-Colmou K, Jouglar E, Pietri M, Chiavassa S, Delpon G, Paris F, Supiot S. Tumor vasculature remodeling by radiation therapy increases doxorubicin distribution and efficacy. Cancer Lett 2019;457:1-9.
12. Nafissi N, Mohammadlou M, Akbari ME, Mahdavi SR, Sheikh M, Borji M, Babaee E, Baharlou R. The impact of intraoperative radiotherapy on breast cancer: focus on the levels of angiogenic factors. World J Surg Oncol 2022;20:191.
13. Yamazaki T, Young KH. Effects of radiation on tumor vasculature. Mol Carcinog 2022;61:165-72.
14. Jain RK. Normalization of tumor vasculature: an emerging concept in antiangiogenic therapy. Science 2005;307:58-62.
15. Wong PP, Bodrug N, Hodivala-Dilke KM. Exploring Novel Methods for Modulating Tumor Blood Vessels in Cancer Treatment. Curr Biol 2016;26:R1161-6.
16. Li W, Quan YY, Li Y, Lu L, Cui M. Monitoring of tumor vascular normalization: the key points from basic research to clinical application. Cancer Manag Res 2018;10:4163-72.
17. Kim E, Stamatelos S, Cebulla J, Bhujwalla ZM, Popel AS, Pathak AP. Multiscale imaging and computational modeling of blood flow in the tumor vasculature. Ann Biomed Eng 2012;40:2425-41.
18. Hoyt K, Umphrey H, Lockhart M, Robbin M, Forero-Torres A. Ultrasound imaging of breast tumor perfusion and neovascular morphology. Ultrasound Med Biol 2015;41:2292-302.
19. Fu Q, Zhu R, Song J, Yang H, Chen X. Photoacoustic Imaging: Contrast Agents and Their Biomedical Applications. Adv Mater 2019;31:e1805875.
20. Luke GP, Yeager D, Emelianov SY. Biomedical applications of photoacoustic imaging with exogenous contrast agents. Ann Biomed Eng 2012;40:422-37.
21. Borg RE, Rochford J. Molecular Photoacoustic Contrast Agents: Design Principles & Applications. Photochem Photobiol 2018;94:1175-209.
22. Manohar S, Dantuma M. Current and future trends in photoacoustic breast imaging. Photoacoustics 2019;16:100134.
23. Abeyakoon O, Woitek R, Wallis MG, Moyle PL, Morscher S, Dahlhaus N, Ford SJ, Burton NC, Manavaki R, Mendichovszky IA, Joseph J, Quiros-Gonzalez I, Bohndiek SE, Gilbert FJ. An optoacoustic imaging feature set to characterise blood vessels surrounding benign and malignant breast lesions. Photoacoustics 2022;27:100383.
24. Oraevsky AA, Clingman B, Zalev J, Stavros AT, Yang WT, Parikh JR. Clinical optoacoustic imaging combined with ultrasound for coregistered functional and anatomical mapping of breast tumors. Photoacoustics 2018;12:30-45.
25. Sun J, Li X, Chen A, Cai W, Peng X, Li L, Fan B, Wang L, Zhang H, Zhang R. A Dual-Modality MR/PA Imaging Contrast Agent Based on Ultrasmall Biopolymer Nanoparticles for Orthotopic Hepatocellular Carcinoma Imaging. Int J Nanomedicine 2019;14:9893-904.
26. Li Y, Ye F, Zhang S, Ni W, Wen L, Qin H. Carbon-Coated Magnetic Nanoparticle Dedicated to MRI/Photoacoustic Imaging of Tumor in Living Mice. Front Bioeng Biotechnol 2021;9:800744.
27. Kakolyris S, Giatromanolaki A, Koukourakis M, Leigh IM, Georgoulias V, Kanavaros P, Sivridis E, Gatter KC, Harris AL. Assessment of vascular maturation in non-small cell lung cancer using a novel basement membrane component, LH39: correlation with p53 and angiogenic factor expression. Cancer Res 1999;59:5602-7.
28. Sorace AG, Quarles CC, Whisenant JG, Hanker AB, McIntyre JO, Sanchez VM, Yankeelov TE. Trastuzumab improves tumor perfusion and vascular delivery of cytotoxic therapy in a murine model of HER2+ breast cancer: preliminary results. Breast Cancer Res Treat 2016;155:273-84.
29. Vangestel C, Van de Wiele C, Van Damme N, Staelens S, Pauwels P, Reutelingsperger CP, Peeters M. (99)mTc-(CO)(3) His-annexin A5 micro-SPECT demonstrates increased cell death by irinotecan during the vascular

normalization window caused by bevacizumab. J Nucl Med 2011;52:1786-94.
30. Song MN, Moon PG, Lee JE, Na M, Kang W, Chae YS, Park JY, Park H, Baek MC. Proteomic analysis of breast cancer tissues to identify biomarker candidates by gel-assisted digestion and label-free quantification methods using LC-MS/MS. Arch Pharm Res 2012;35:1839-47.
31. Braun RD, Bissig D, North R, Vistisen KS, Berkowitz BA. Human tumor cell proliferation evaluated using manganese-enhanced MRI. PLoS One 2012;7:e30572.
32. Saito S, Hasegawa S, Sekita A, Bakalova R, Furukawa T, Murase K, Saga T, Aoki I. Manganese-enhanced MRI reveals early-phase radiation-induced cell alterations in vivo. Cancer Res 2013;73:3216-24.
33. Marusyk A, Polyak K. Tumor heterogeneity: causes and consequences. Biochim Biophys Acta 2010;1805:105-17.
34. Junttila MR, de Sauvage FJ. Influence of tumour microenvironment heterogeneity on therapeutic response. Nature 2013;501:346-54.
35. Lan J, Wan XL, Deng L, Xue JX, Wang LS, Meng MB, Ling H, Zhang X, Mo XM, Lu Y. Ablative hypofractionated radiotherapy normalizes tumor vasculature in lewis lung carcinoma mice model. Radiat Res 2013;179:458-64.
36. Clément-Colmou K, Potiron V, Pietri M, Guillonneau M, Jouglar E, Chiavassa S, Delpon G, Paris F, Supiot S. Influence of Radiotherapy Fractionation Schedule on the Tumor Vascular Microenvironment in Prostate and Lung Cancer Models. Cancers (Basel) 2020.
37. Benjamin LE, Golijanin D, Itin A, Pode D, Keshet E. Selective ablation of immature blood vessels in established human tumors follows vascular endothelial growth factor withdrawal. J Clin Invest 1999;103:159-65.
38. Hellevik T, Martinez-Zubiaurre I. Radiotherapy and the tumor stroma: the importance of dose and fractionation. Front Oncol 2014;4:1.
39. Roy S, Kumaravel S, Sharma A, Duran CL, Bayless KJ, Chakraborty S. Hypoxic tumor microenvironment: Implications for cancer therapy. Exp Biol Med (Maywood) 2020;245:1073-86.
40. Rey S, Schito L, Koritzinsky M, Wouters BG. Molecular targeting of hypoxia in radiotherapy. Adv Drug Deliv Rev 2017;109:45-62.
41. Harrison H, Pegg HJ, Thompson J, Bates C, Shore P. HIF1-alpha expressing cells induce a hypoxic-like response in neighbouring cancer cells. BMC Cancer 2018;18:674.
42. Rakotomalala A, Escande A, Furlan A, Meignan S, Lartigau E. Hypoxia in Solid Tumors: How Low Oxygenation Impacts the "Six Rs" of Radiotherapy. Front Endocrinol (Lausanne) 2021;12:742215.
43. Orlova A, Pavlova K, Kurnikov A, Maslennikova A, Myagcheva M, Zakharov E, Skamnitskiy D, Perekatova V, Khilov A, Kovalchuk A, Moiseev A, Turchin I, Razansky D, Subochev P. Noninvasive optoacoustic microangiography reveals dose and size dependency of radiation-induced deep tumor vasculature remodeling. Neoplasia 2022;26:100778.
44. Syed AK, Whisenant JG, Barnes SL, Sorace AG, Yankeelov TE. Multiparametric Analysis of Longitudinal Quantitative MRI data to Identify Distinct Tumor Habitats in Preclinical Models of Breast Cancer. Cancers (Basel) 2020;12:1682.
45. Filatenkov A, Baker J, Mueller AM, Kenkel J, Ahn GO, Dutt S, Zhang N, Kohrt H, Jensen K, Dejbakhsh-Jones S, Shizuru JA, Negrin RN, Engleman EG, Strober S. Ablative Tumor Radiation Can Change the Tumor Immune Cell Microenvironment to Induce Durable Complete Remissions. Clin Cancer Res 2015;21:3727-39.
46. Ostrand-Rosenberg S, Horn LA, Ciavattone NG. Radiotherapy Both Promotes and Inhibits Myeloid-Derived Suppressor Cell Function: Novel Strategies for Preventing the Tumor-Protective Effects of Radiotherapy. Front Oncol 2019;9:215.
47. Fu SY, Chen FH, Wang CC, Yu CF, Chiang CS, Hong JH. Role of Myeloid-Derived Suppressor Cells in High-Dose-Irradiated TRAMP-C1 Tumors: A Therapeutic Target and an Index for Assessing Tumor Microenvironment. Int J Radiat Oncol Biol Phys 2021;109:1547-58.
48. Yang G, Kong Q, Wang G, Jin H, Zhou L, Yu D, Niu C, Han W, Li W, Cui J. Low-dose ionizing radiation induces direct activation of natural killer cells and provides a novel approach for adoptive cellular immunotherapy. Cancer Biother Radiopharm 2014;29:428-34.
49. Lei QQ, Sui JD, Jin F, Luo HL, Shan JJ, Tang L, Wang Y, Wu YZ. Impact of high-dose rate radiotherapy on B and natural killer (NK) cell polarization in peripheral blood mononuclear cells (PBMCs) via inducing non-small cell lung cancer (NSCLC)-derived exosomes. Transl Cancer Res 2021;10:3538-47.
50. Yin T, Xin H, Yu J, Teng F. The role of exosomes in tumour immunity under radiotherapy: eliciting abscopal effects? Biomark Res 2021;9:22.
51. Nishikawa H, Koyama S. Mechanisms of regulatory T cell infiltration in tumors: implications for innovative immune precision therapies. J Immunother Cancer 2021;9:e002591.
52. Gupta A, Probst HC, Vuong V, Landshammer A, Muth S, Yagita H, Schwendener R, Pruschy M, Knuth A, van den

Broek M. Radiotherapy promotes tumor-specific effector CD8+ T cells via dendritic cell activation. J Immunol 2012;189:558-66.
53. Belgiovine C, Digifico E, Anfray C, Ummarino A, Torres Andón F. Targeting Tumor-Associated Macrophages in Anti-Cancer Therapies: Convincing the Traitors to Do the Right Thing. J Clin Med 2020;9:3226.
54. Wu M, Huang Q, Xie Y, Wu X, Ma H, Zhang Y, Xia Y. Improvement of the anticancer efficacy of PD-1/PD-L1 blockade via combination therapy and PD-L1 regulation. J Hematol Oncol 2022;15:24.
55. Deng L, Liang H, Burnette B, Beckett M, Darga T, Weichselbaum RR, Fu YX. Irradiation and anti-PD-L1 treatment synergistically promote antitumor immunity in mice. J Clin Invest 2014;124:687-95.
56. Yi M, Zheng X, Niu M, Zhu S, Ge H, Wu K. Combination strategies with PD-1/PD-L1 blockade: current advances and future directions. Mol Cancer 2022;21:28.
57. Demaria S, Guha C, Schoenfeld J, Morris Z, Monjazeb A, Sikora A, Crittenden M, Shiao S, Khleif S, Gupta S, Formenti SC, Vikram B, Coleman CN, Ahmed MM. Radiation dose and fraction in immunotherapy: one-size regimen does not fit all settings, so how does one choose? J Immunother Cancer 2021;9:e002038.
58. Dewan MZ, Galloway AE, Kawashima N, Dewyngaert JK, Babb JS, Formenti SC, Demaria S. Fractionated but not single-dose radiotherapy induces an immune-mediated abscopal effect when combined with anti-CTLA-4 antibody. Clin Cancer Res 2009;15:5379-88.
59. Arina A, Gutiontov SI, Weichselbaum RR. Radiotherapy and Immunotherapy for Cancer: From "Systemic" to "Multisite". Clin Cancer Res 2020;26:2777-82.

Cite this article as: Xu N, Wu D, Gao J, Jiang H, Li Q, Bao S, Luo Y, Zhou Q, Liao C, Yang J. The effect of tumor vascular remodeling and immune microenvironment activation induced by radiotherapy: quantitative evaluation with magnetic resonance/photoacoustic dual-modality imaging. Quant Imaging Med Surg 2023;13(10):6555-6570. doi: 10.21037/qims-23-229

